water

MDPI

Article

Fast Prediction of Solitary Wave Forces on Box-Girder Bridges Using Artificial Neural Networks

Minglong Lu [1], Shaopeng Li [2] and Teng Wu [3,*]

[1] Department of Bridge Engineering, School of Civil Engineering, Central South University, Changsha 410075, China
[2] Department of Civil and Coastal Engineering, University of Florida, Gainesville, FL 32603, USA
[3] Department of Civil, Structural and Environmental Engineering, University at Buffalo, Buffalo, NY 14126, USA
* Correspondence: tengwu@buffalo.edu

Abstract: The extreme shallow-water waves during a tropical cyclone are often simplified to solitary waves. Considering the lack of simulation tools to effectively and efficiently forecast wave forces on coastal box-girder bridges during tropical cyclones, this study investigates the impacts of solitary waves on box girders and accordingly develops a fast prediction model for solitary wave forces. Computational fluid dynamics (CFD) simulations are used to simulate the hydrodynamic forces on the bridge deck. A total of 368 cases are calculated for the parametric study by varying the submergence coefficients (C_s), relative wave heights (H/h) and deck aspect ratios (W/h). With the CFD simulation results as the training datasets, an artificial neural network (ANN) is trained utilizing the back-propagation algorithm. The maximum wave forces first increase and then decrease with the C_s, while they monotonically increase with H/h. For relatively large H/h and small C_s values, the relationship between the maximum wave forces and W/h presents strong nonlinearities. The observed correlation coefficients between the ANN predictions and the CFD results for the vertical and horizontal wave forces are 98.6% and 98.1%, respectively. The trained ANN-based model shows good prediction accuracy and could be used as an efficient model for the tropical cyclone risk analysis of coastal bridges.

Keywords: solitary wave; hydrodynamic force; coastal bridge; artificial neural networks

check for updates

Citation: Lu, M.; Li, S.; Wu, T. Fast Prediction of Solitary Wave Forces on Box-Girder Bridges Using Artificial Neural Networks. *Water* **2023**, *15*, 1963. https://doi.org/10.3390/w15101963

Academic Editor: Bommanna Krishnappan

Received: 14 April 2023
Revised: 10 May 2023
Accepted: 18 May 2023
Published: 22 May 2023

1. Introduction

Severe storm surges and waves can be generated by a high-speed wind blowing across the surface of the ocean over a long period of time during a tropical cyclone [1–3]. Among various types of coastal infrastructure, low-clearance bridges (with box girders) can be vulnerable to high waves. While the water-level and wave-height rise caused by a tropical cyclone can be significant [1,4–6], the clearance level of non-navigable coastal bridges is relatively low [7,8]. However, many existing low-clearance coastal box-girder bridges were designed without considering the loads from surges and waves, posing a serious threat to the safety of the bridge superstructure. Coastal bridges play a crucial role in the transportation infrastructure network in terms of both during-a disaster response and post-disaster recovery. To help stakeholders make informed decisions, it is of critical importance to develop an effective and efficient approach to evaluating wave-induced hydrodynamic loads on coastal bridges.

After Hurricanes Ivan and Katrina causing damage to many coastal bridges in the US [9–11], numerous researchers began to investigate the wave forces of coastal bridges [12–21]. The accurate evaluation and efficient prediction of wave forces on coastal bridges have significant applications, such as in structural design and optimization, load mitigation measures, and the emergency response to tropical cyclone hazards. Douglass et al. [22] developed an empirical method for computing wave loads on bridge superstructures.

Based on the Douglass formula, McPherson [23] considered the increase in the wave forces of the bridge caused by the entrapped air. In addition, Kulicki and Mertz [24] considered the effects of wave height, wave period, wavelength and bridge type on wave forces. Furthermore, several researchers focused on solitary waves and developed formulas for determining the wave forces on bridge superstructures [25–29]. In general, the wave forces on the bridge decks are related to the still water level, wave type, wave height, wave period, and size of the structure. In addition, the coupling effects of waves and structures present significant nonlinearities [30–36]. Hence, the simulation accuracy of wave forces based on the existing empirical or semi-empirical formulas needs to be further improved. While the numerical simulations using computational fluid dynamics (CFD) and experimental testing in a wave tank can be considered as two reliable tools to investigate the wave forces on coastal bridges, they are very time-consuming and expensive, which is not suitable for risk-informed decision-making involving the simulation of many different scenarios. Hence, it is beneficial to develop a surrogate model with high prediction efficiency.

Artificial neural networks (ANNs) have been widely used as surrogate models in many disciplines [37–39]. Once trained, the feedforward operations in ANNs are very efficient at making predictions. In ocean engineering, ANNs have been applied to forecast wave forces on different structures [40–42]; however, few studies have examined the application of ANNs in the prediction of wave forces on coastal bridges. Xu et al. [43] considered the still water level (SWL), bottom elevation of the girder/superstructure, and wave height as the inputs to the ANN model for wave force predictions. The accuracy of their ANN model is measured by the root mean squared error (RMSE) and the correlation coefficient (R). The values of RMSE/F_{V_mean} and RMSE/F_{H_mean} were 4.05% and 6.28%, where F_{V_mean} and F_{H_mean} represent the mean values of the maximum vertical and horizontal forces, respectively. The correction coefficients between their ANN prediction and the CFD data for the vertical and horizontal forces were 0.99 and 0.995, respectively. The R values closer to 1 and smaller RMSE values represent a better predictive performance of the ANN model. Based on data from 3D CFD simulations, taking water depth, wave height, clearance, wave velocity, wave period, wavelength, and wave steepness as inputs, Zhu et al. [21] obtained an ANN model that predicts wave forces. Furthermore, Xu et al. [44] developed a novel ensemble model for the prediction of wave forces on coastal bridge decks. Jia et al. [45] also found that the ANN model presented a good performance in predicting wave forces in the longitudinal direction. It is noted that all these studies were limited to a specific bridge deck and hence did not account for the effect of different bridge geometries on wave forces.

Since the height of waves continues to increase with a shape similar to that of solitary waves as the extreme waves travel into the shallow water [2], the solitary wave is often used to analyze the impacts on the coastal infrastructure from near-shore waves [46,47]. Considering the lack of simulation tools to accurately and efficiently predict the wave forces on box girders (with different configurations and loading conditions), this study aims to develop an efficient reduced-order model for the assessment of wave forces on typical coastal low-clearance box-girder bridges. Specifically, the maximum wave forces on the box girders with various girder widths, wave heights, and submersion coefficients are first determined through the CFD simulations. The effects of the water depth, wave height, and deck width on the maximum wave force are investigated. Then, an ANN is developed as the surrogate model using the CFD datasets. The comparison of ANN predictions and CFD simulations suggests that the developed surrogate model can accurately predict the wave forces with high efficiency.

2. Numerical Model and Validation

Figure 1 shows the schematic diagram for the two-dimensional computational domain (180 m in length by 20 m in height), where SWL is the still water level that separates the regions of the air and water at the initial condition, H is the solitary wave height, and d is the still water depth. For the boundary conditions, AC is set as the velocity inlet, AB and BD are, respectively, set as the pressure inlet and outlet, and CD is set as the no-slip stationary wall condition.

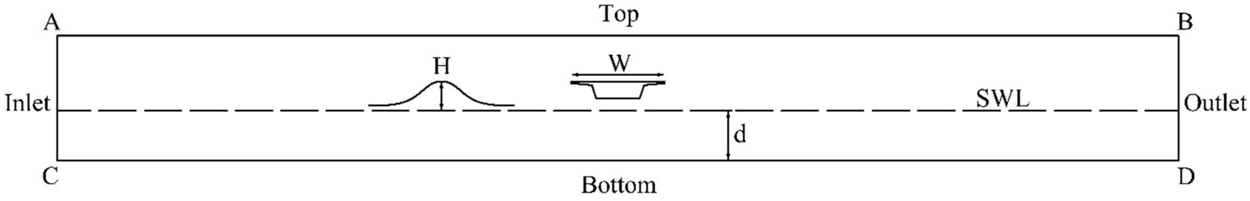

Figure 1. Computational domain and boundary conditions.

2.1. Governing Equations

In the computational domain, the incompressible water is assumed to satisfy the Reynolds-averaged Navier–Stokes (RANS) equations. For two-dimensional simulations, the mass and momentum conservation equations for the fluid are, accordingly, as follows:

$$\frac{\partial(\overline{u}_i)}{\partial x_i} = 0 \tag{1}$$

$$\rho\frac{\partial\overline{u}_i}{\partial t} + \rho\partial\overline{u}_j\frac{\partial\overline{u}_i}{\partial x_j} = -\frac{\partial\overline{p}}{\partial x_i} + \mu\frac{\partial^2\overline{u}_i}{\partial x_i\partial x_j} - \frac{\partial\rho\overline{u_i'u_j'}}{\partial x_j} \tag{2}$$

where $\overline{u}_i$ and $\overline{u}_j$ are the average velocities in the i and j directions, respectively; u_i' and u_j' are the fluctuation velocities along the i and j directions, respectively; x_i and x_j are the coordinate axes along the i and j directions, respectively; $\overline{p}$ is the average pressure; ρ is the density of fluid; μ is the viscosity of fluid; and t is the time. To determine the dynamic free surface for a two-phase flow issue, the volume of fluid (VOF) method is used [48].

In this study, the commercial CFD software Fluent 2020R2 is employed to simulate solitary wave–bridge deck interactions. The spatial domain is discretized utilizing the finite volume method (FVM) and the turbulence is modelled using the shear-stress transport (SST) k-ω scheme, where k is the turbulence kinetic energy and ω is the specific dissipation. The nondimensional wall-coordinate $y+$ is smaller than 5 to obtain the reliable pressure and velocity fields in the near-wall regions. The Pressure-Implicit with Splitting of Operators (PISO) scheme is used for the pressure–velocity coupling, and the PRESTO! scheme is selected for the pressure spatial discretization. The least squares cell-based scheme is employed for gradient discretization, the second-order upwind scheme for momentum advection terms, the compressive scheme for volume fraction equations, and the second-order implicit scheme for transient formulation.

2.2. Solitary Wave Generation and Elimination

The key to velocity inlet wave generation is to simulate the velocity field and wave surface at the inlet boundary. When the waves travel to shallow-water regions, they are distorted by changes in water depth with amplified nonlinearity. Noting that the shape of the solitary wave is similar to the shallow water wave, the solitary wave is often used to analyze the shallow-water wave for the sake of simplicity. The solitary wave equations used by Chen et al. [49] can be expressed as follows:

$$\eta = Hsech^2\left[\sqrt{\frac{3H}{4d^3}}(x-ct)\right] \tag{3}$$

$$u = \sqrt{gd}\frac{H}{d}sech^2\left[\sqrt{\frac{3H}{4d^3}}(x-ct)\right] \tag{4}$$

$$v = \sqrt{3gd}\left(\frac{H}{d}\right)^{1.5}\frac{z}{d}sech^2\left[\sqrt{\frac{3H}{4d^3}}(x-ct)\right]\tanh\left[\sqrt{\frac{3H}{4d^3}}(x-ct)\right] \tag{5}$$

$$c = \sqrt{gd}\left[1+\frac{H}{d}(-1+2)\right]^{\frac{1}{2}} = \sqrt{g(d+H)} \tag{6}$$

where η is the distance from the wave surface to the still water level; c is the wave celerity; H is the wave height; d is the still water level (SWL); and g is the acceleration of gravity. To generate the solitary waves, a User Define Function (UDF) composed of Equations (3)–(6) at $x = 0$ (boundary conditions of the inlet) is programmed in Fluent 2020R2 based on the target water depth and wave height. The solitary waves will be accordingly generated in the numerical wave flume by solving the governing equations. To prevent the waves from reflecting back to affect the incident waves, a wave elimination zone is set before the exit boundary of the numerical water tank with an artificial damping source added to the momentum equations. The artificial damping is linearly proportional to the water velocity, with a damping coefficient defined as [50]:

$$\delta(x) = \beta\frac{x-x_1}{L_s} \tag{7}$$

where L_s is the length of the wave elimination zone with $L_s = x_1 - x_2$; x_1 and x_2 are the start and end coordinates of the wave elimination zone; and $x_1 \leq x \leq x_2$; β is an empirical parameter.

2.3. Validation of Numerical Wave Flume

With an appropriate inlet velocity and wave elimination, the two-dimensional numerical wave tank with a length of 180 m and a height of 20 m is established and the solitary waves can be generated accordingly. Wave gauges are positioned at 0 m, 45 m, 90 m, and 135 m to measure the fluctuations of the wave surface. The comparison between the numerical and theoretical solutions is shown in Figure 2, and the corresponding errors between the wave heights at 45 m, 90 m, and 135 m are presented in Table 1. It is clear that the numerical simulations are close to the theoretical solutions, which verifies the accuracy of the numerical wave flume.

Table 1. The errors between theoretical and numerical wave heights with 5 m water depth.

Location	Numerical Wave Height	Theoretical Wave Height	Error
45 m	2.528 m	2.5 m	1.12%
90 m	2.502 m	2.5 m	0.08%
135 m	2.477 m	2.5 m	0.92%

2.4. Validation of Numerical Wave Force

The validation of the numerical wave flume simply suggests that the CFD model can generate solitary waves with sufficient accuracy. To further prove that the CFD model can accurately simulate hydrodynamic loads on the structures, it is also desirable to compare the numerically obtained wave forces with those obtained from experiments. The experiments conducted by Seiffert et al. [51] are used here for the purpose of hydrodynamics validation. The dimensions of the plate used in Seiffert et al. [51] are 30.48 cm in width and 1.27 cm in height. The depth of the water is 8.60 cm, the solitary wave height is 2.47 cm, and the submergence depth is 1.72 cm (measured from the level of the still water to the top of the plate). In the experiment conducted by Seiffert et al. [52], the dimensions of the T-type girder are 30.48 cm in width and 5.08 cm in height. The water depth is 7.1 cm, the solitary wave height is 3.55 cm, and the model elevation is 3.905 cm (measured from the still water level to the bottom of the bridge deck). Figures 3 and 4 depict the comparison results between the wave forces obtained using the current CFD model and the experiments of Seiffert et al. [51,52]. As presented in Figures 3 and 4, the CFD simulation results are close to the experimental data. Due to the use of RANS equations, the numerical results may not capture the high-frequency fluctuations in the wave forces well, which is not of significance in the static response analysis of bridge deck under wave forces. Furthermore, the good agreements suggest that the CFD model can accommodate various structural types (e.g., plate or T-type deck) and submerged conditions (e.g., structures underwater or above water). Therefore, the developed CFD model can be reliably used to accurately estimate the wave forces on various bridge decks.

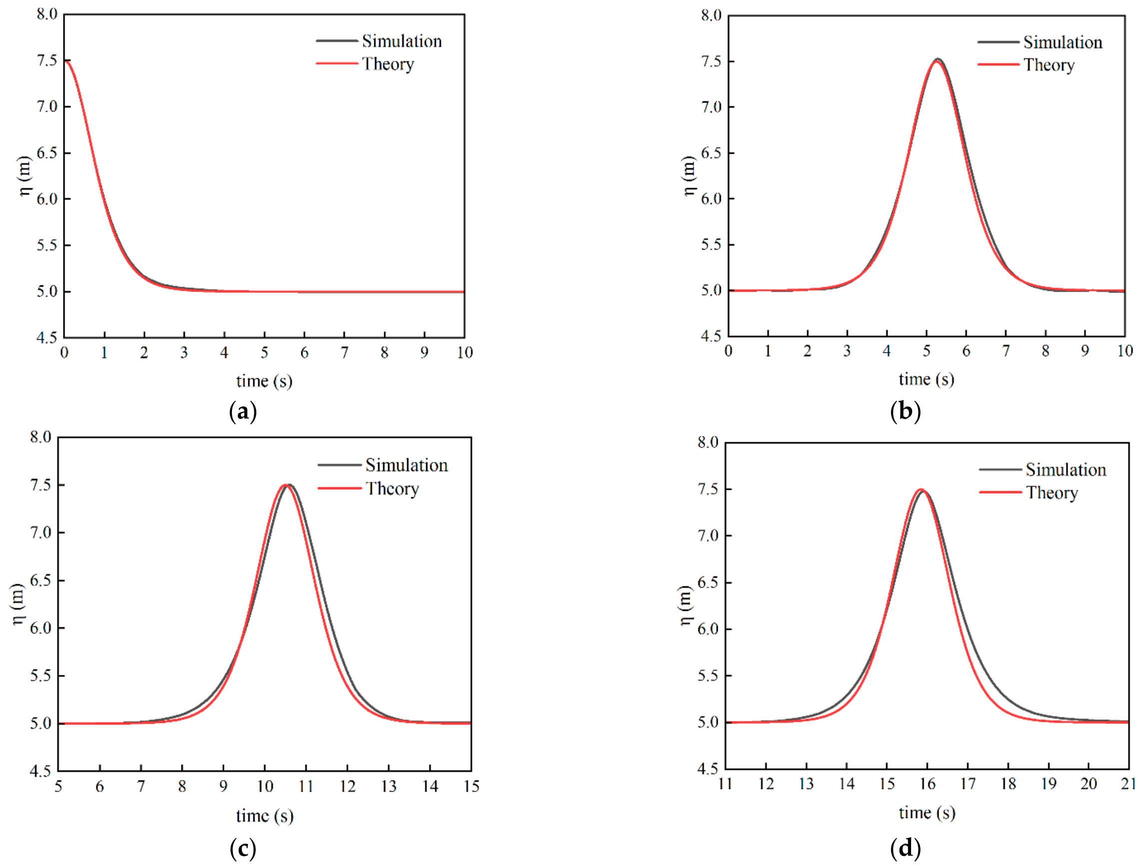

Figure 2. Free surface profiles for solitary waves at various locations: (**a**) 0 m; (**b**) 45 m; (**c**) 90 m; (**d**) 135 m.

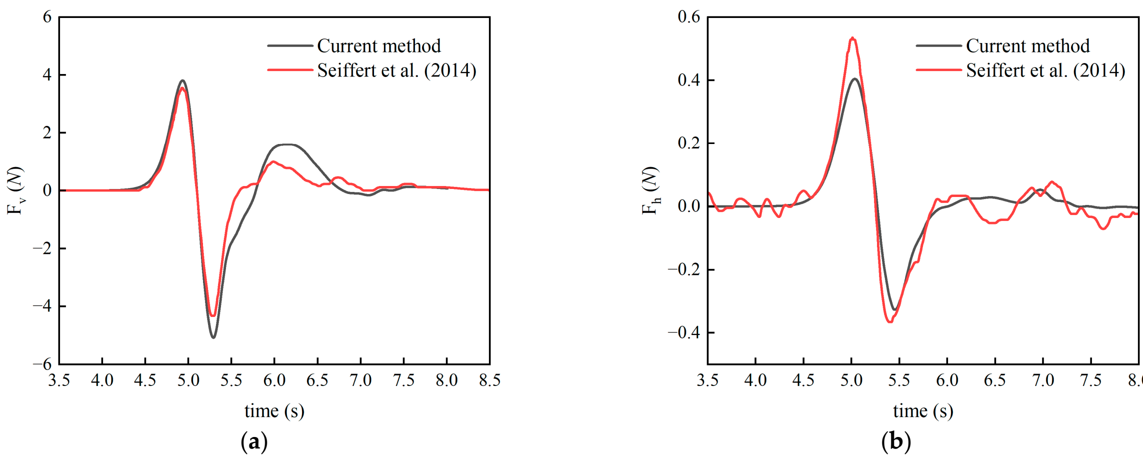

Figure 3. Comparisons of wave forces by CFD model and Seiffert et al. [51]: (**a**) vertical wave forces; (**b**) horizontal wave forces.

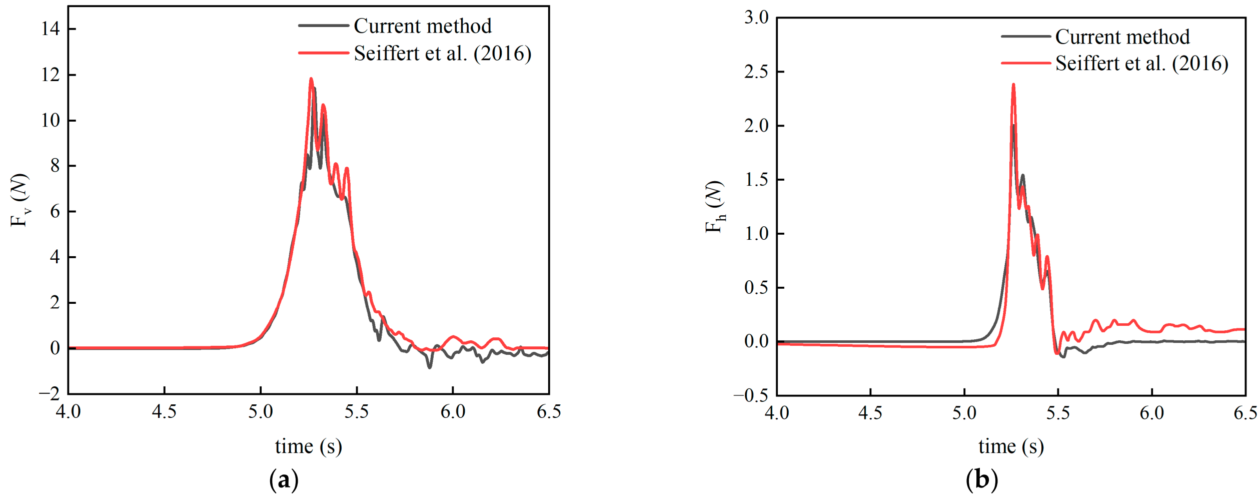

Figure 4. Comparisons of wave forces by the CFD model and Seiffert et al. [52]: (**a**) vertical wave forces; (**b**) horizontal wave forces.

3. Numerical Results and Parametric Study

The prototype deck in this study originates from a typical coastal bridge, as shown in Figure 5. The structure has a width of 15 m, a girder height of 2.1 m, a girder width of 7 m, and a deck thickness of 0.6 m. The computational domain is divided into three regions, from left to right: the near inlet zone, the near deck zone, and the near outlet zone. Figure 6 presents a schematic representation of the mesh zones within the computational domain. To ensure the accuracy of the adopted mesh system, a mesh independency study is performed by refining the mesh size until no major changes in the simulation results are noted. The mesh size for the near inlet zone, near deck zone, and near outlet zone are set to 0.5 m, 0.05 m, and 0.5 m, respectively. In addition, mesh sizes of 0.35 m, 0.05 m, and 0.3 m are employed for the air zone, wave surface zone, and deep-water zone, respectively. Near the wall boundaries, a smaller mesh set is used to ensure all y+ values are less than 5. In addition, the time discretization method is adaptive so that the courant number is always smaller than 0.25.

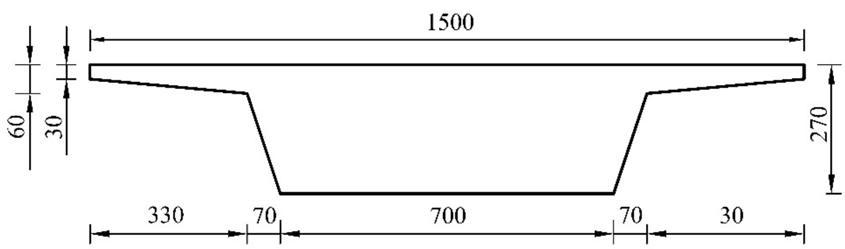

Figure 5. Geometric dimensions of the bridge deck (unit: cm).

The interaction between the wave and the box girder is a complicated nonlinear process. The vertical force F_v and horizontal force F_h on the bridge deck are the functions of the wave and bridge characteristics [53]:

$$F_i = f(W, L_d, h, d_r, Z_c, Z_{ele}, d, H, c, g, \rho, \alpha, \mu) \tag{8}$$

where the subscript i denotes v or h; the bridge deck width (W), deck length (L_d), deck height (h), rail height (d_r), deck clearance (Z_c), and bottom elevation of the bridge superstructure (Z_{ele}) are the bridge parameters; the wave parameters are the wave height (H), wave celerity (c), angle of incidence to the structure (α), water depth (d), water density (ρ), and dynamic viscosity (μ).

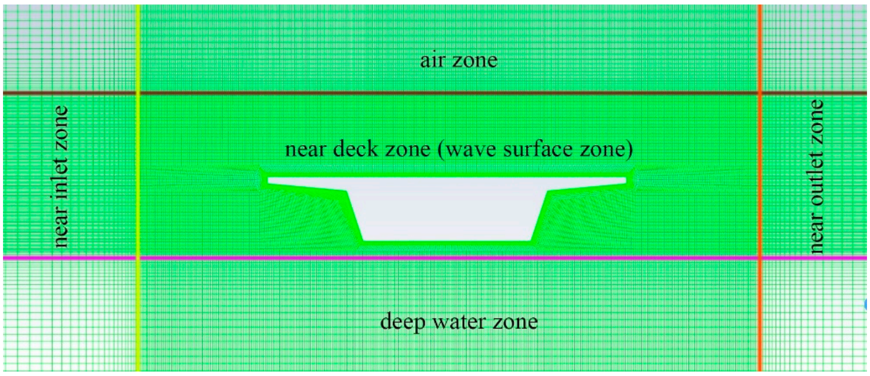

Figure 6. Mesh zones within computational domain.

In this study, the rail height (d_r) is ignored for the sake of simplicity and the deck length (L_d) can be treated as unity for two-dimensional scenarios. Both the water density (ρ) and the dynamic viscosity (μ) are constant. In addition, the deck height (h) of the model is 2.7 m, the bottom elevation of the bridge superstructure (Z_{ele}) is 6 m, and the angle of incidence to the structure (α) is 90 degrees. The deck clearance (Z_c) can be calculated by Z_{ele} and the water depth (d). The wave celerity (C) is related to the wave height (H). As a result, the vertical force, F_v, and horizontal force, F_h, on the bridge deck are investigated by highlighting the influence of the parameters d, H, and W on the solitary wave forces.

3.1. Solitary Wave Force on Bridge Deck

Figure 7 presents a typical time history of numerically obtained vertical wave forces acting on the box girder. The submergence coefficient C_S is defined as the submergence depths $(Z^* = d - Z_{ele})$ divided by the deck height (h), where $C_S = 0$ and $C_S = 1$ respectively indicating that the SWL is equal to the bottom of the girder and the top of the deck. The simulation results suggest that the solitary wave forces consist of two components, namely a slamming force and a quasi-static force. In Figure 7, t_1 and t_2 represent the time instants of maximum slamming force and quasi-static force, respectively. The box girder is subject to a slamming force several times greater than the maximum quasi-static force due to the existence of the flat plate, and the short-duration slamming force occurs slightly before the peak of the quasi-static force. In addition to the uplift wave force, it is noted that the box girder may suffer from a significant downward wave force.

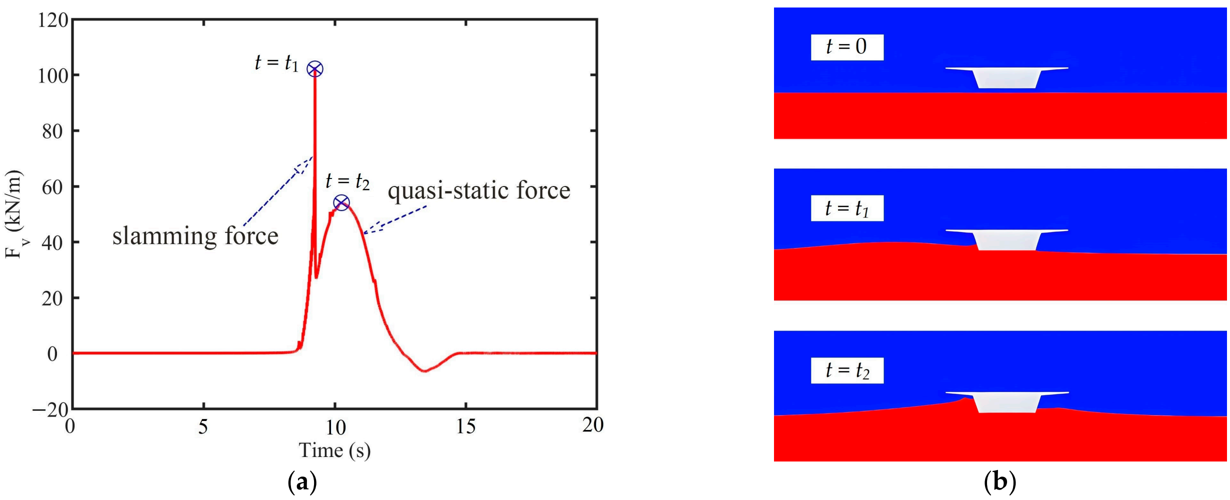

Figure 7. Vertical wave force on the bridge deck with $C_s = -0.185$, H = 1.5 m, and W = 15 m: (**a**) wave force time history; (**b**) snapshot of the wave–deck interaction.

3.2. Parametric Study on Wave Force

The effects of the water depth (d) on the maximum wave forces are investigated in terms of the submergence coefficient (C_S). As shown in Figure 8, both the maximum vertical and horizontal wave forces converge around $C_S = 0.8$. While there is always a significant increase in the vertical wave forces until they reach their peak values, a similar phenomenon is not observed for the horizontal wave forces with relatively small W/h and/or H/h values (e.g., $W/h = 4.074$ and/or $H/h = 0.556$). For $H/h = 0.556$ and $H/h = 0.741$, the peak value of maximum vertical wave forces is achieved at approximately $C_S = 0.35$. For $H/h = 0.926$ and $H/h = 1.111$, the peak value of maximum vertical wave forces is achieved at approximately $C_S = 0.2$.

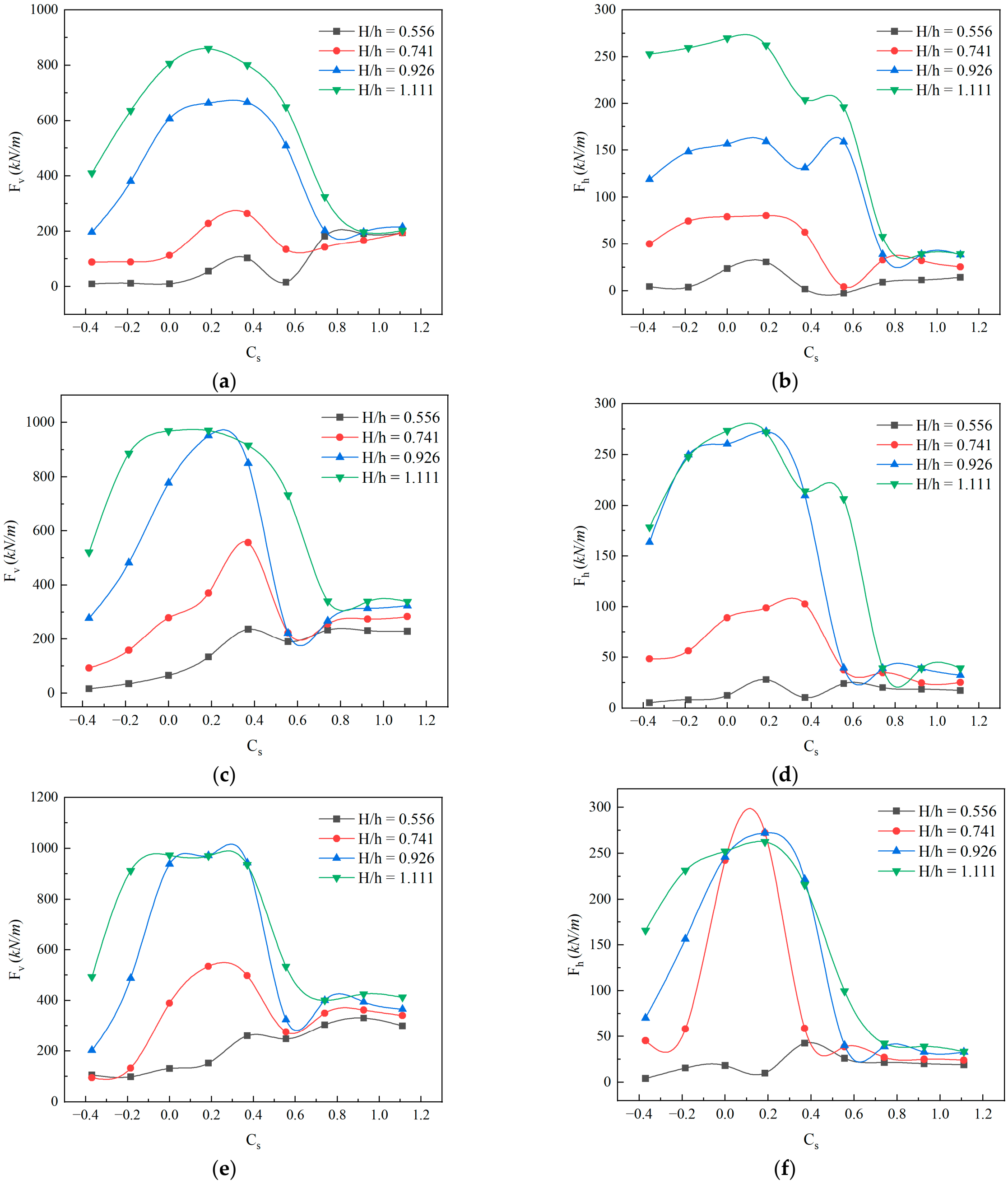

Figure 8. The relationship between the maximum wave force and submergence coefficient: (**a**) vertical wave force for W/h = 4.074; (**b**) horizontal wave force for W/h = 4.074; (**c**) vertical wave force for W/h = 4.815; (**d**) horizontal wave force for W/h = 4.815; (**e**) vertical wave force for W/h = 5.556; (**f**) horizontal wave force for W/h = 5.556.

The effects of the wave height (H) on the maximum wave forces are investigated in terms of the relative wave height (H/h). As shown in Figure 9, both the maximum vertical and horizontal wave forces monotonically increase with respect to the relative wave height. The relationship between the maximum wave forces and relative wave heights presents high nonlinearities for small C_s. On the other hand, the maximum wave force increases relative to the wave height following an approximately linear relationship for large C_s (e.g., $C_s = 1$).

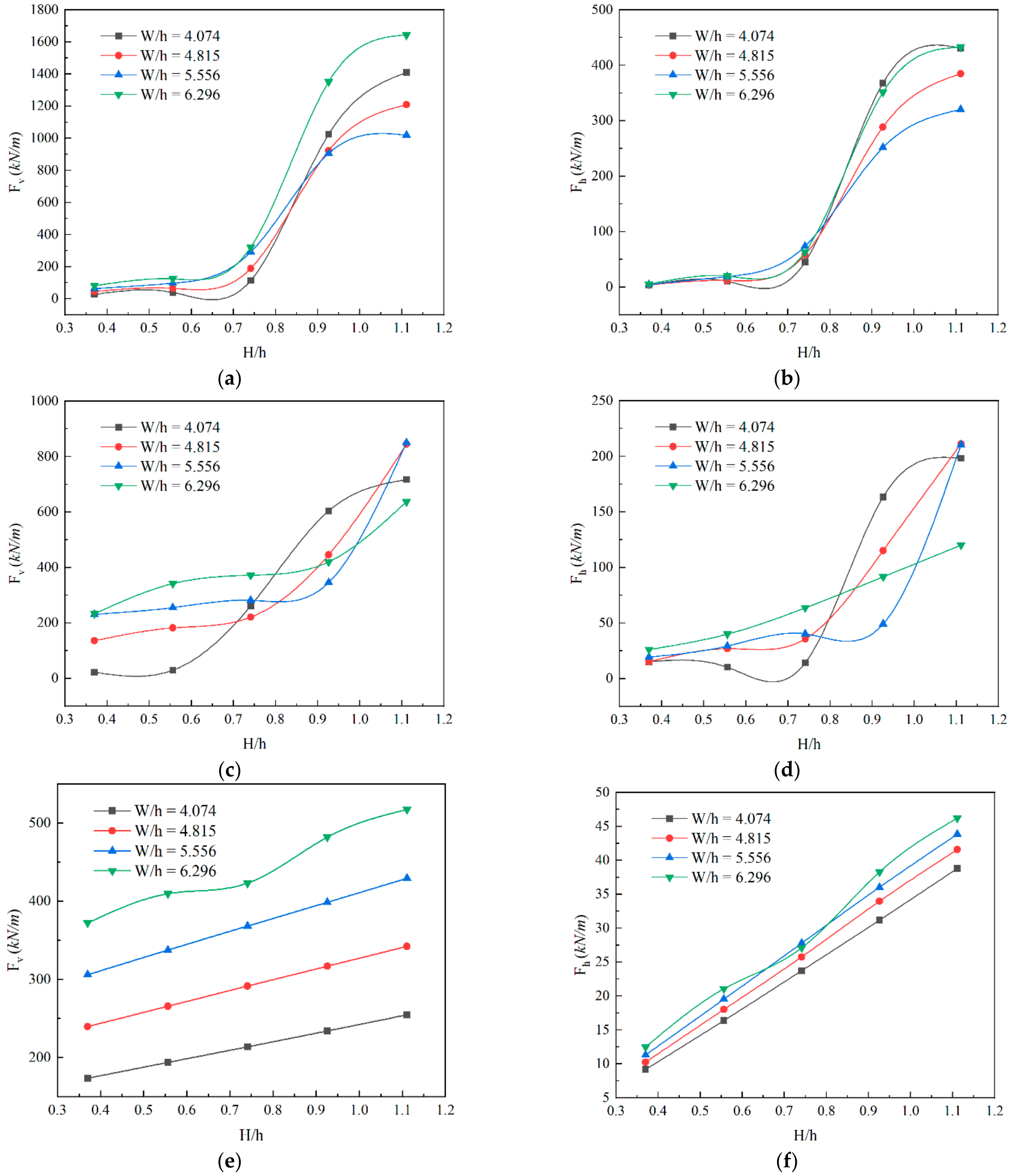

Figure 9. The relationship between the maximum wave force and relative wave height: (**a**) vertical wave force for $C_s = 0$; (**b**) horizontal wave force for $C_s = 0$; (**c**) vertical wave force for $C_s = 0.5$; (**d**) horizontal wave force for $C_s = 0.5$; (**e**) vertical wave force for $C_s = 1$; (**f**) horizontal wave force for $C_s = 1$.

The effects of the deck width (W) on the maximum wave forces are investigated in terms of the deck aspect ratio (W/h). As shown in Figure 10, both the maximum vertical and horizontal wave forces linearly increase with W/h for relatively small H/h and/or large C_s values (e.g., H/h = 0.37 and/or C_s = 1). For the relatively small values of C_s, however, the relationship between the maximum wave forces and deck aspect ratios presents strong nonlinearities at relatively large values of H/h.

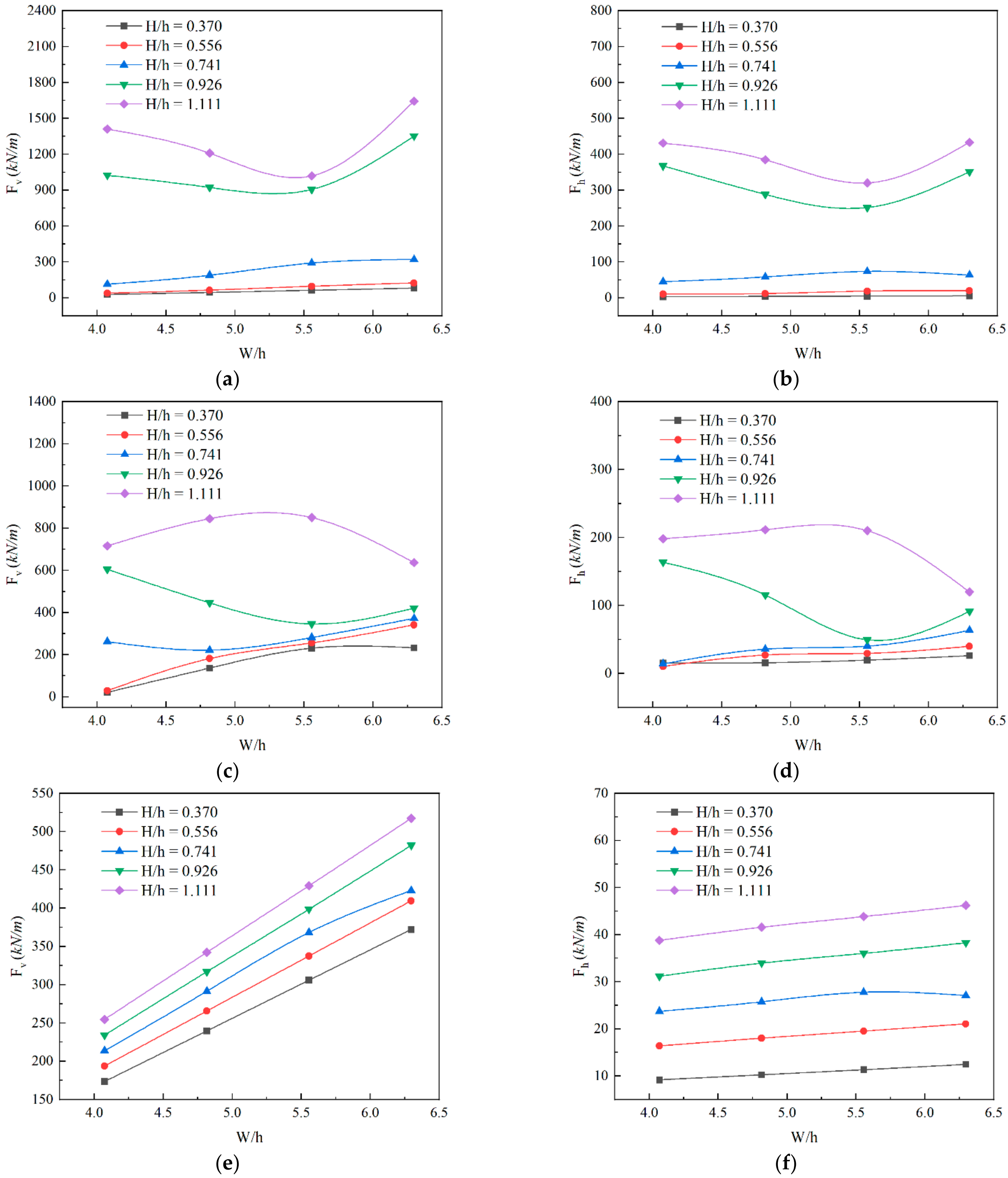

Figure 10. The relationship between the maximum wave force and deck aspect ratio: (**a**) vertical wave force for C_s = 0; (**b**) horizontal wave force for C_s = 0; (**c**) vertical wave force for C_s = 0.5; (**d**) horizontal wave force for C_s = 0.5; (**e**) vertical wave force for C_s = 1; (**f**) horizontal wave force for C_s = 1.

4. Artificial Neural Network for Fast Prediction of Wave Force

The artificial neural network (ANN), inspired by the biological neural network in human brains, can conduct mathematical operations to predict output with given input through connected layers of artificial neurons. There are three types of layers in a typical ANN, namely the input layer, hidden layers, and the output layer. The adjacent layers are connected with weights and biases. Through training from prepared datasets, the ANN learns the appropriate weights and biases to minimize the difference between the prediction and the ground truth (from the training data), which has shown great potential for complicated nonlinear problems. In this study, the ANN is used to rapidly predict the maximum wave forces on bridge decks with various submergence coefficients, relative wave heights, and deck aspect ratios.

4.1. Datasets

A total of 368 CFD simulations, with various inputs of submergence coefficients, relative wave heights and deck aspect ratios, are performed to generate the corresponding outputs of maximum wave forces on the bridge decks. The obtained comprehensive datasets can be used to train an ANN. Table 2 lists the upper and lower bounds of inputs and outputs for these 368 cases. For the sake of clarity, all the maximum wave forces in the datasets are shown in Figure 11 as a function of submersion coefficient, relative wave height or deck aspect ratio.

Table 2. Input and output range in the datasets.

Parameter	Minimum	Maximum
Submersion coefficient	−0.370	1.111
Relative wave height	0.370	1.111
Aspect ratio	4.074	6.296
Vertical force	9.200 kN/m	1643.2 kN/m
Horizontal force	1.720 kN/m	654.77 kN/m

4.2. Training Process

The process for training an ANN is schematically shown in Figure 12. A batch of training data is fed to the network at the input layer, in which C_s, H/h, and W/h refer to the submersion coefficient, relative wave height, and deck aspect ratio, respectively. The summation sign ($\sum$) denotes $C_s \cdot W_{1i}^{(I)} + (W/h) \cdot W_{2i}^{(I)} + (H/h) \cdot W_{3i}^{(I)}$, where $W_{1i}^{(I)}$, $W_{2i}^{(I)}$, and $W_{3i}^{(I)}$ are the weights from the input layer neurons to the ith neurons in the first hidden layer, and b_i is the bias for the ith neurons in the first hidden layer. This summation will go through a nonlinear active function and obtain an "activated" value of h_i^1 as the input for the next hidden layer. This feedforward procedure will repeat until the Mth layer (where M is the total hidden layer number) and obtain the prediction of the output F (i.e., the maximum wave forces F_v or F_h).

The loss function at the output neuron is defined as:

$$Loss = \frac{1}{2}\sum_{k=1}^{K}(T_k - O_k)^2 \tag{9}$$

where K is the total number of data points in the datasets and T_k and O_k denote the target and output values, respectively. The loss function (capturing the differences between the prediction and the ground truth) evaluates the predicting accuracy of the ANN model. The backpropagation algorithm is used to dynamically update the weights of the connections between two adjacent layers using the gradient descent method to minimize the loss function [43]. This iteration will continue until the ANN achieves the expected performance.

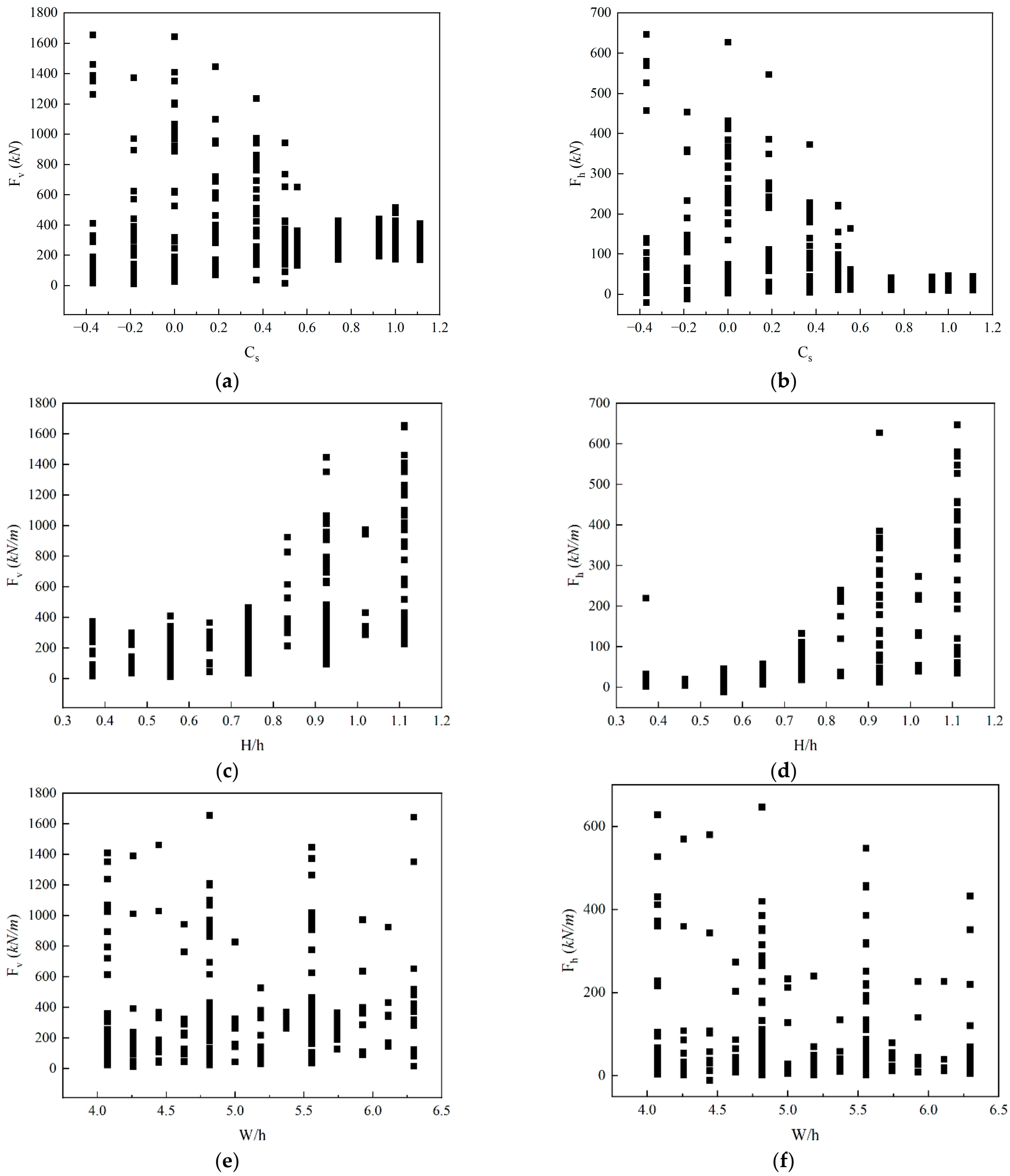

Figure 11. The maximum wave forces in datasets: (**a**) vertical wave forces resulting from various submersion coefficients; (**b**) horizontal wave forces resulting from various submersion coefficients; (**c**) vertical wave forces resulting from various relative wave heights; (**d**) horizontal wave forces resulting from various relative wave heights; (**e**) vertical wave forces resulting from various deck aspect ratios; (**f**) horizontal wave forces resulting from various deck aspect ratios.

Two ANNs using the Adam optimizer with a batch size of 30 are built for the simulation of maximum vertical and horizontal wave forces, respectively, and the corresponding hyperparameters are fine-tuned based on trial and error. Specifically, the number of hidden layers is 3 in the ANN for vertical wave force simulations, and the numbers of neurons in the first, second, and third hidden layers are 88, 40, and 10, respectively. On the other hand, the number of hidden layers is also 3 in the ANN for horizontal wave force simulations, and the numbers of neurons in the first, second, and third hidden layers are 190, 40, and 10, respectively. For both ANNs, the activation function of the first and second hidden layers is Tanh while that of the third hidden layer is ReLU.

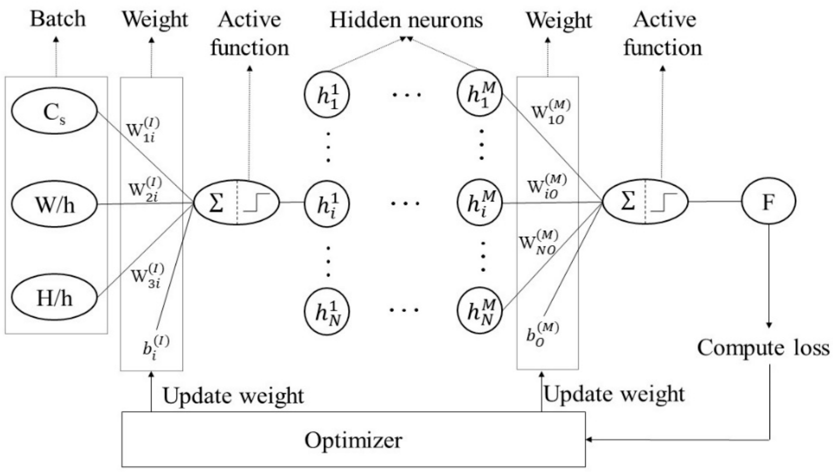

Figure 12. ANN training process.

4.3. Prediction Accuracy

Using the abovementioned network architectures, the loss function values for the training dataset (80 percent of the total data points) is depicted in Figure 13, where the full dataset iterates over 4000 epochs. Once the ANN is well trained, it can be used to rapidly predict the maximum wave forces on the bridge decks. The correlation coefficient ®is used to evaluate the model performance, defined as follows:

$$R = \frac{\sum_{k=1}^{K} (T_k - \overline{T})(O_k - \overline{O})}{\sum_{k=1}^{K} (T_k - \overline{T})^2 \sum_{k=1}^{K} (O_k - \overline{O})^2} \tag{10}$$

where the overbar denotes the mean value. The proximity of R to 1.0 indicates good prediction accuracy. For the testing dataset (20 percent of the total data points), Figure 14 compares the ANN predictions with the CFD simulations for all input combinations of C_s, H/h, and W/h. The observed correlation coefficient (R) between the prediction and ground truth for the vertical and horizontal wave forces are 98.6% and 98.1%, respectively. The comparisons between the ANN predictions and the CFD simulations for selected C_s, H/h, and W/h values are shown in Figure 15. These comparison results suggest that the proposed ANN-based surrogate model can accurately capture both vertical and horizontal wave forces on various bridge decks.

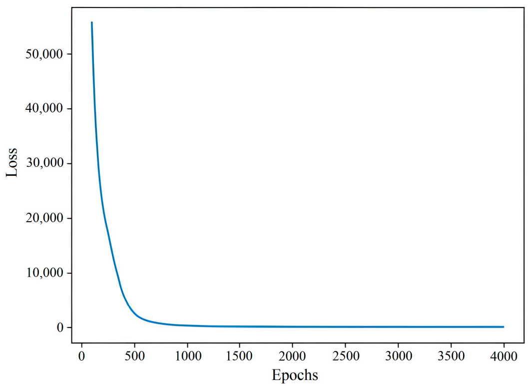

(**a**)

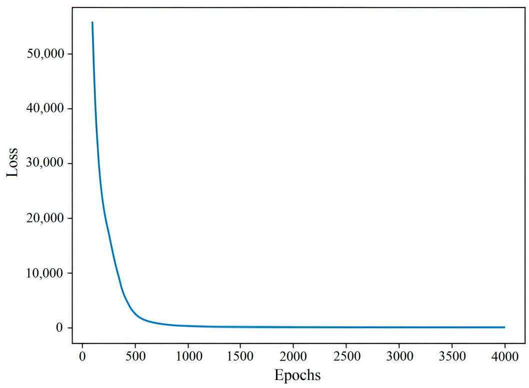

(**b**)

Figure 13. Training process: (**a**) vertical force; (**b**) horizontal force.

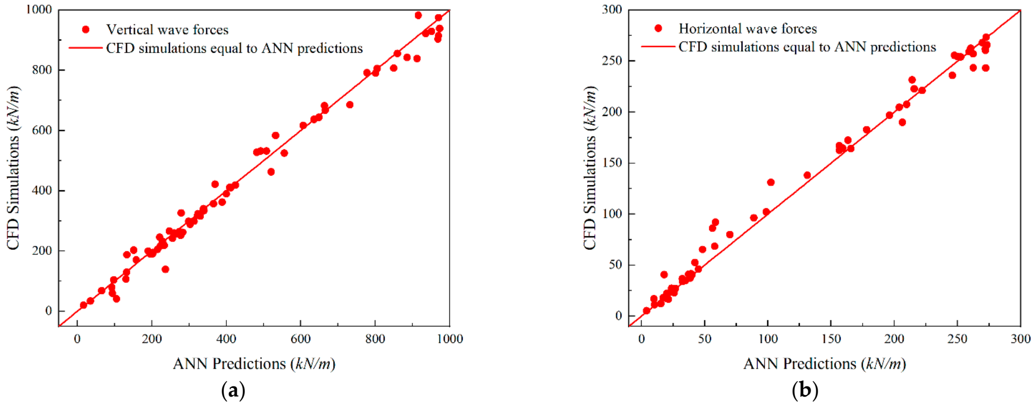

Figure 14. Correlation coefficient: (**a**) vertical wave force; (**b**) horizontal wave force.

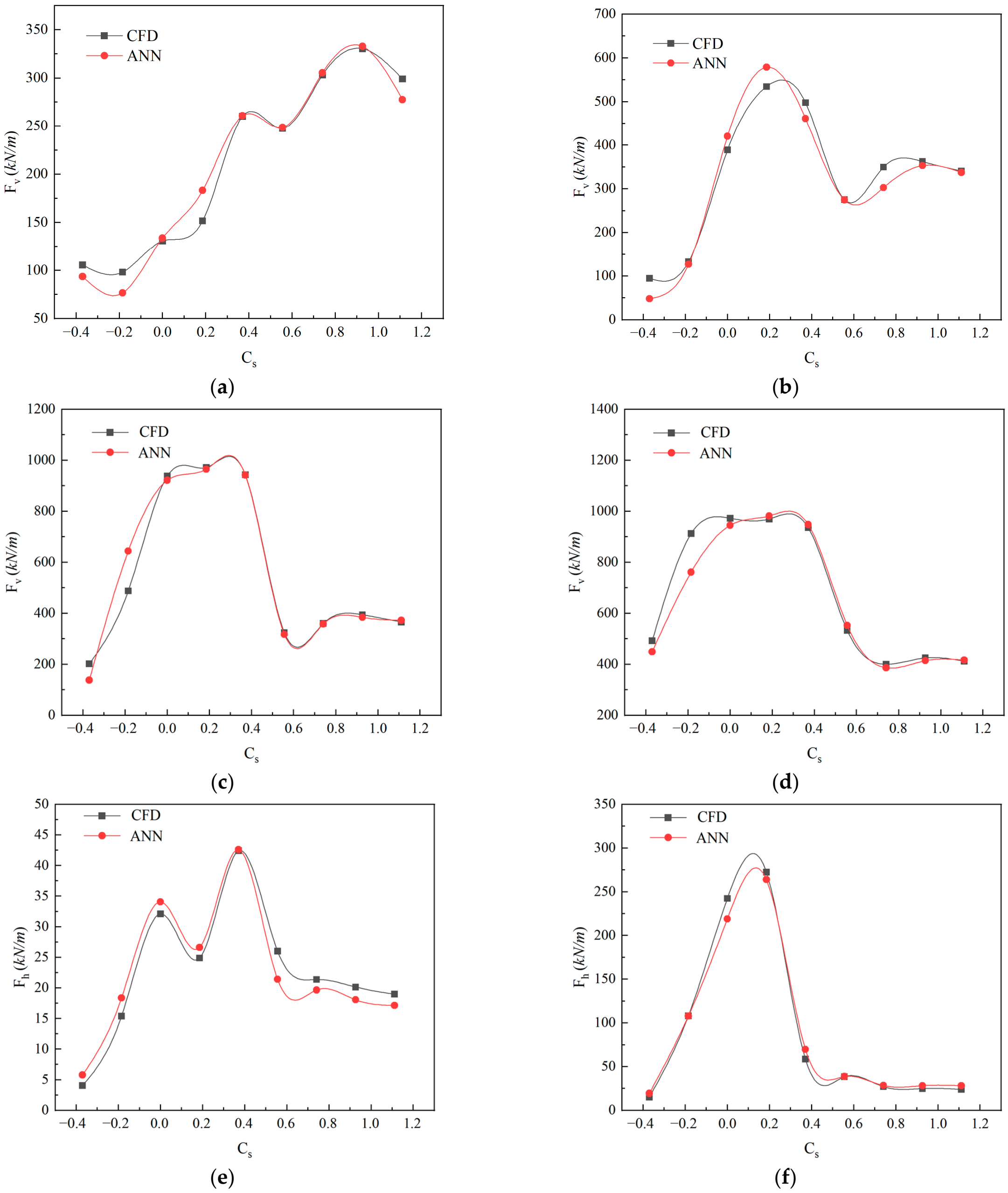

Figure 15. *Cont.*

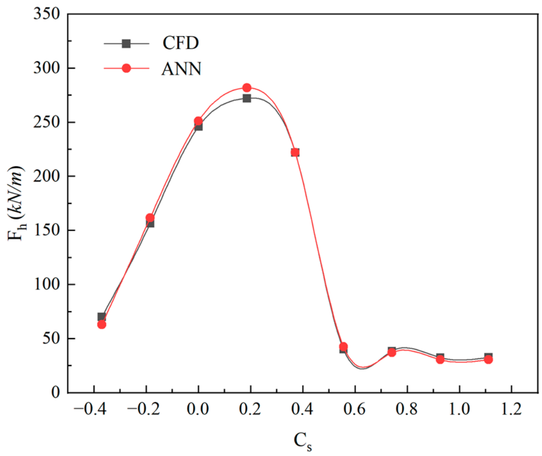

(**g**)

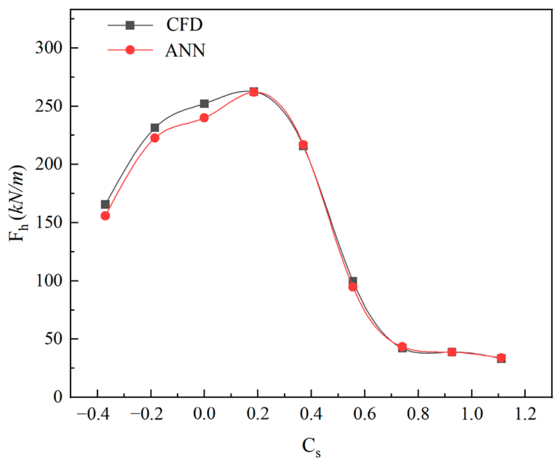

(**h**)

Figure 15. The comparison between ANN predictions and CFD simulations: (**a**) vertical wave force for W/h = 5.556 and H/h = 0.556; (**b**) vertical wave force for W/h = 5.556 and H/h = 0.741; (**c**) vertical wave force for W/h = 5.556 and H/h = 0.926; (**d**) vertical wave force for W/h = 5.556 and H/h = 1.111; (**e**) horizontal wave force for W/h = 5.556 and H/h = 0.556; (**f**) horizontal wave force for W/h = 5.556 and H/h = 0.741; (**g**) horizontal wave force for W/h = 5.556 and H/h = 0.926; (**h**) horizontal wave force for W/h = 5.556 and H/h = 1.111.

5. Conclusions and Future Directions

This study first developed CFD simulations of tropical cyclone-induced wave forces on the decks of coastal box-girder bridges. In the case where the wave crest struck the box girder or flange plate, both the slamming wave force and quasi-static wave force were observed in the vertical (uplift) direction. The CFD simulations were then used to train an ANN-based surrogate model in the fast prediction of maximum wave forces. The main conclusions are as follows:

(1) Both the maximum vertical and horizontal wave forces first increased and then decreased with the submersion coefficient C_s, and finally converged around C_s = 0.8. The peak values of maximum vertical wave forces were achieved in the range of C_s equal to 0.2–0.35, depending on the relative wave height (H/h) and the deck aspect ratio (W/h). For the maximum positive horizontal wave forces, the peak values were obtained in the range of C_s equal to 0–0.2.

(2) Both the maximum vertical and horizontal wave forces monotonically increased with respect to H/h. The relationship between the maximum wave forces and relative wave heights presented strong nonlinearities for small C_s. On the other hand, the maximum wave force increased with H/h following an approximately linear relationship for large C_s. Both the maximum vertical and horizontal wave forces linearly increased with W/h for relatively small H/h and large C_s values. For relatively large H/h and small C_s values, however, the relationship between the maximum wave forces and deck aspect ratios presented strong nonlinearities.

(3) The ANN model efficiently and accurately predicted wave forces on bridge decks for various C_s, H/h, and W/h values.

It is noted that the solitary wave–bridge deck interactions are extremely complex and highly nonlinear. In addition to the deck aspect ratio, relative wave height and submersion coefficient, other parameters, such as the inclination angle of the box girder web, corner point height, and girder height need further examination. Furthermore, the hydrodynamic forces induced by more realistic surface waves (e.g., irregular waves and broken waves) should be investigated in future studies. The destructive power of tropical cyclones is not limited to a single direction, and hence bridge performance under various wave propagation directions also requires further investigation.

Author Contributions: Conceptualization, T.W.; Methodology, M.L. and T.W.; Validation, M.L.; Data curation, M.L.; Writing—original draft, M.L.; Writing—review and editing, S.L. and T.W. All authors have read and agreed to the published version of the manuscript.

Funding: This work was supported by the Innovation-Driven Project of Central South University (No. 2020CX009) and the Institute of Bridge Engineering at University at Buffalo.

Data Availability Statement: All data are available from the corresponding author by request.

Conflicts of Interest: The authors declare no conflict of interest.

Nomenclature

C_s	Submergence coefficients
H	Wave height
h	Height of bridge deck
W	Width of bridge deck
H/h	Relative wave height
W/h	Deck aspect ratio
RMSE	Root mean squared error
F_{V_mean}	Mean values for the maximum vertical wave force
F_{H_mean}	Mean values for the maximum horizontal wave force
d	Still water depth
$\overline{u}_i$	Average velocity in the *i* direction
$\overline{u}_j$	Average velocity in the *j* direction
u'_i	Fluctuation velocity along the *i* direction
u'_j	Fluctuation velocity along the *j* direction
x_i	Coordinate axis along the *i* direction
x_j	Coordinate axis along the *j* direction
$\overline{p}$	Average pressure
ρ	Density of fluid
μ	Viscosity of fluid
t	Time
k	Turbulence kinetic energy
ω	Dissipation
$y+$	Nondimensional wall-coordinate
η	Distance from the wave surface to the still water level
c	Wave celerity
x	Axis of horizontal direction
z	Axis of vertical direction
g	Gravity acceleration
$\delta(x)$	Damping coefficient
L_s	Length of the wave elimination zone
x_1	Start coordinates of the wave elimination zone
x_2	End coordinates of the wave elimination zone
β	Empirical parameter of the damping coefficient
F_v	Maximum vertical wave force
F_h	Maximum horizontal wave force
L_d	Deck length
d_r	Height of rail
Z_c	Clearance of bridge deck
Z_{ele}	Bottom elevation of the bridge superstructure
α	Angle of incidence to the structure
Z^*	Submergence depths
t_1	Time of maximum slamming force
t_2	Time of maximum quasi-static force
t_3	Time of maximum downward force
$W_{1i}^{(I)}$, $W_{2i}^{(I)}$, $W_{3i}^{(I)}$	Weights from the input layer neurons to the *i*th neurons in the first hidden layer
b_i	Bias for the *i*th neurons in the first hidden layer
h_i^1	The "activated" value of the *i*th neurons in the first hidden layer

T_k	Target value
O_k	Output value
R	Correlation coefficient
$\overline{T}$	Mean of the target value
$\overline{O}$	Mean of the output value

References

1. Roeber, V.; Bricker, J.D. Destructive tsunami-like wave generated by surf beat over a coral reef during Typhoon Haiyan. *Nat. Commun.* **2015**, *6*, 7854. [CrossRef] [PubMed]
2. Hansom, J.D.; Switzer, A.D.; Pile, J. Extreme waves: Causes, characteristics, and impact on coastal environments and society. In *Coastal and Marine Hazards, Risks, and Disasters*; Shroder, J.F., Ellis, J.T., Sherman, D.J., Eds.; Elsevier: Amsterdam, The Netherlands, 2015; pp. 307–334.
3. Yin, J.; Griffies, S.M.; Winton, M.; Zhao, M.; Zanna, L. Response of Storm-Related Extreme Sea Level along the U.S. Atlantic Coast to Combined Weather and Climate Forcing. *J. Clim.* **2020**, *33*, 3745–3769. [CrossRef]
4. Hansom, J.; Barltrop, N.; Hall, A. Modelling the processes of cliff-top erosion and deposition under extreme storm waves. *Mar. Geol.* **2008**, *253*, 36–50. [CrossRef]
5. Wang, D.-P.; Oey, L.-Y. Hindcast of Waves and Currents in Hurricane Katrina. *Bull. Am. Meteorol. Soc.* **2008**, *89*, 487–496. [CrossRef]
6. Wang, D.W.; Mitchell, D.A.; Teague, W.J.; Jarosz, E.; Hulbert, M.S. Extreme waves under hurricane Ivan. *Science* **2005**, *309*, 896. [CrossRef]
7. Chen, H.C.; Liu, L.; Liu, X.D.; Zhou, S.S. Overall Design of East Man-Made Island Junction Bridge of Hongkong-Zhuhai-Macao Bridge. *World Bridge* **2016**, *3*, 1–5.
8. Ge, L.-Z.; Chen, H.-B.; Chen, S.-G.; Liu, H.Y. Experimental Study on Wave Forces Acting on Bridge at the Junction of Island and Bridge in the Shenzhen-Zhongshan Channel West Artificial Island. In Proceedings of the the 30th International Ocean and Polar Engineering Conference, Virtual, 11–16 October 2020.
9. Okeil, A.M.; Cai, C. Survey of short-and medium-span bridge damage induced by Hurricane Katrina. *J. Bridge Eng.* **2008**, *13*, 377–387. [CrossRef]
10. Padgett, J.; DesRoches, R.; Nielson, B.; Yashinsky, M.; Kwon, O.-S.; Burdette, N.; Tavera, E. Bridge damage and repair costs from Hurricane Katrina. *J. Bridge Eng.* **2008**, *13*, 6–14. [CrossRef]
11. Huang, W.; Xiao, H. Numerical modeling of dynamic wave force acting on Escambia Bay Bridge deck during Hurricane Ivan. *J. Waterw. Port Coast. Ocean Eng.* **2009**, *135*, 164–175. [CrossRef]
12. Bozorgnia, M.; Lee, J.-J. Wave Structure Interaction during Hurricane Ivan Simulated by Two-Phase Flow Model. In Proceedings of the Engineering Mechanics Conference, Los Angeles, CA, USA, 8–11 August 2011; pp. 33–44.
13. Bradner, C.; Schumacher, T.; Cox, D.; Higgins, C. Experimental setup for a large-scale bridge superstructure model subjected to waves. *J. Waterw. Port Coast. Ocean Eng.* **2011**, *137*, 3–11. [CrossRef]
14. Hayatdavoodi, M.; Seiffert, B.; Ertekin, R.C. Experiments and calculations of cnoidal wave loads on a flat plate in shallow-water. *J. Ocean Eng. Mar. Energy* **2015**, *1*, 77–99. [CrossRef]
15. Huang, B.; Zhu, B.; Cui, S.; Duan, L.; Zhang, J. Experimental and numerical modelling of wave forces on coastal bridge superstructures with box girders, Part I: Regular waves. *Ocean Eng.* **2018**, *149*, 53–77. [CrossRef]
16. Jin, J.; Meng, B. Computation of wave loads on the superstructures of coastal highway bridges. *Ocean Eng.* **2011**, *38*, 2185–2200. [CrossRef]
17. Marin, J.; Sheppard, D.M. Storm surge and wave loading on bridge superstructures. In Proceedings of the Structures Congress 2009, Austin, TX, USA, 30 April–2 May 2009; pp. 1–10.
18. Seiffert, B.R.; Hayatdavoodi, M.; Ertekin, R.C. Experiments and calculations of cnoidal wave loads on a coastal-bridge deck with girders. *Eur. J. Mech. B/Fluids* **2015**, *52*, 191–205. [CrossRef]
19. Xu, G.; Cai, C. Numerical investigation of the lateral restraining stiffness effect on the bridge deck-wave interaction under Stokes waves. *Eng. Struct.* **2017**, *130*, 112–123. [CrossRef]
20. Yuan, P.; Xu, G.; Chen, Q.; Cai, C. Framework of practical performance evaluation and concept of interface design for bridge deck–wave interaction. *J. Bridge Eng.* **2018**, *23*, 04018048. [CrossRef]
21. Zhu, D.; Li, Y.; Dong, Y. Reliability-based retrofit assessment of coastal bridges subjected to wave forces using 3D CFD simulation and metamodeling. *Civ. Eng. Environ. Syst.* **2021**, *38*, 59–83. [CrossRef]
22. Douglass, S.L.; Chen, Q.; Olsen, J.; Edge, B.; Brown, D. *Wave Forces on Bridge Decks*; Department of Transportation, Federal Highway Administration, Office of Bridge Technology: Washington, DC, USA, 2006.
23. McPherson, R.L. *Hurricane Induced Wave and Surge Forces on Bridge Decks*; Texas A & M University: College Station, TX, USA, 2010.
24. Kulicki, J.M.; Mertz, D.R. *Guide Specifications for Bridges Vulnerable to Coastal Storms*; American Association of State Highway and Transportation Officials: Washington, DC, USA, 2008.
25. Azadbakht, M.; Yim, S.C. Simulation and estimation of tsunami loads on bridge superstructures. *J. Waterw. Port Coast. Ocean Eng.* **2015**, *141*, 04014031. [CrossRef]

26. Xiang, T.; Istrati, D.; Yim, S.C.; Buckle, I.G.; Lomonaco, P. Tsunami loads on a representative coastal bridge deck: Experimental study and validation of design equations. *J. Waterw. Port Coast. Ocean Eng.* **2020**, *146*, 04020022. [CrossRef]
27. Xu, G.; Cai, C.; Deng, L. Numerical prediction of solitary wave forces on a typical coastal bridge deck with girders. *Struct. Infrastruct. Eng.* **2017**, *13*, 254–272. [CrossRef]
28. Yim, S.C.; Boon-Intra, S.; Nimmala, S.B.; Winston, H.M.; Azadbakht, M.; Cheung, K.F. *Development of a Guideline for Estimating Tsunami Forces on Bridge Superstructures*; OR-RD-12-03; Oregon Department of Transportation, Research Section: Multnomah, WA, USA, 2011; pp. 35–38.
29. Zhu, D.; Dong, Y. Experimental and 3D numerical investigation of solitary wave forces on coastal bridges. *Ocean Eng.* **2020**, *209*, 107499. [CrossRef]
30. Xu, F.; Wu, T.; Ying, X.; Kareem, A. Higher-order self-excited drag forces on bridge decks. *J. Eng. Mech.* **2016**, *142*, 06015007. [CrossRef]
31. Abbas, N.; Shatanawi, W.; Rehman, K.U.; Shatnawi, T.A. Velocity and thermal slips impact on boundary layer flow of micropolar nanofluid over a vertical nonlinear stretched Riga sheet. *Proc. Inst. Mech. Eng. Part N J. Nanomater. Nanoeng. Nanosyst.* **2023**, 1. [CrossRef]
32. Zhang, M.; Wu, T.; Xu, F. Vortex-induced vibration of bridge decks: Describing function-based model. *J. Wind Eng. Ind. Aerodyn.* **2019**, *195*, 104016. [CrossRef]
33. Abbas, N.; Shatanawi, W.; Shatnawi, T.A. Theoretical analysis of modified non-Newtonian micropolar nanofluid flow over vertical Riga sheet. *Int. J. Mod. Phys. B* **2023**, *37*, 2350016. [CrossRef]
34. Wu, T.; Kareem, A. Modelling of nonlinear bridge aerodynamics and aeroelasticity: A convolution based approach. In *MATEC Web of Conferences*; EDP Sciences: Les Ulis, France, 2012; Volume 1, p. 03004.
35. Abbas, N.; Malik, M.Y.; Nadeem, S. Stagnation flow of hybrid nanoparticles with MHD and slip effects. *Heat Transf.Asian Res.* **2020**, *49*, 180–196. [CrossRef]
36. Wu, T.; Kareem, A.; Li, S. On the excitation mechanisms of rain–wind induced vibration of cables: Unsteady and hysteretic nonlinear features. *J. Wind Eng. Ind. Aerodyn.* **2013**, *122*, 83–95. [CrossRef]
37. Wu, T.; Kareem, A. Modeling hysteretic nonlinear behavior of bridge aerodynamics via cellular automata nested neural network. *J. Wind Eng. Ind. Aerodyn.* **2011**, *99*, 378–388. [CrossRef]
38. Li, S.; Snaiki, R.; Wu, T. A knowledge-enhanced deep reinforcement learning-based shape optimizer for aerodynamic mitigation of wind-sensitive structures. *Comput. -Aided Civ. Infrastruct. Eng.* **2021**, *36*, 733–746. [CrossRef]
39. Wu, T.; Snaiki, R. Applications of machine learning to wind engineering. *Front. Built Environ.* **2022**, *8*, 811460. [CrossRef]
40. Li, L.; Gao, Z.; Yuan, Z.-M. On the sensitivity and uncertainty of wave energy conversion with an artificial neural-network-based controller. *Ocean Eng.* **2019**, *183*, 282–293. [CrossRef]
41. Lotfollahi-Yaghin, M.; Pourtaghi, A.; Sanaaty, B.; Lotfollahi-Yaghin, A. Artificial neural network ability in evaluation of random wave-induced inline force on a vertical cylinder. *China Ocean Eng.* **2012**, *26*, 19–36. [CrossRef]
42. Mase, H.; Kitano, T. Prediction model for occurrence of impact wave force. *Ocean Eng.* **1999**, *26*, 949–961. [CrossRef]
43. Xu, G.; Chen, Q.; Chen, J. Prediction of solitary wave forces on coastal bridge decks using artificial neural networks. *J. Bridge Eng.* **2018**, *23*, 04018023. [CrossRef]
44. Xu, G.; Ji, C.; Wei, H.; Wang, J.; Yuan, P. A novel ensemble model using artificial neural network for predicting wave-induced forces on coastal bridge decks. *Eng. Comput.* **2022**, 1–24. [CrossRef]
45. Jia, L.; Zhang, Y.; Zhu, D.; Dong, Y. 3D Numerical Modeling and Quantification of Oblique Wave Forces on Coastal Bridge Superstructures. *J. Mar. Sci. Eng.* **2022**, *10*, 860. [CrossRef]
46. Berryman, J.G. Stability of solitary waves in shallow water. *Phys. Fluids* **1976**, *19*, 771–777. [CrossRef]
47. Zdyrski, T.; Feddersen, F. Wind-induced changes to surface gravity wave shape in shallow water. *J. Fluid Mech.* **2021**, *913*, A27. [CrossRef]
48. Hirt, C.W.; Nichols, B.D. Volume of fluid (VOF) method for the dynamics of free boundaries. *J. Comput. Phys.* **1981**, *39*, 201–225. [CrossRef]
49. Chen, M.; Huang, B.; Yang, Z.; Ren, Q.; Zhu, B. The Influence of Lateral Restraining Stiffness on the Box-Girder Superstructure under Unbroken Solitary Waves. *J. Mar. Sci. Eng.* **2022**, *10*, 1019. [CrossRef]
50. Park, J.C.; Kim, M.H.; Miyata, H. Fully non-linear free-surface simulations by a 3D viscous numerical wave tank. *Int. J. Numer. Methods Fluids* **1999**, *29*, 685–703. [CrossRef]
51. Seiffert, B.; Hayatdavoodi, M.; Ertekin, R.C. Experiments and computations of solitary-wave forces on a coastal-bridge deck. Part I: Flat plate. *Coast. Eng.* **2014**, *88*, 194–209. [CrossRef]
52. Seiffert, B.R.; Cengiz Ertekin, R.; Robertson, I.N. Effect of Entrapped Air on Solitary Wave Forces on a Coastal Bridge Deck with Girders. *J. Bridge Eng.* **2016**, *21*, 04015036-1–04015036-14. [CrossRef]
53. Sheppard, D.M.; Marin, J. *Wave Loading on Bridge Decks*; BD545-58; Florida Department of Transportation: Tallahassee, FL, USA, 2009; p. 63.